


Quantum interference and occupation control in high harmonic generation from monolayer WS₂

Received: 30 March 2025

Accepted: 21 October 2025

Published online: 06 November 2025

 Check for updates

Minjeong Kim^{1,2,13}, Taeho Kim^{1,2,13}, Anna Galler^{3,4,13}, Dasol Kim¹, Alexis Chacon^{1,5,6,7}, Xiangxin Gong⁸, Yuhui Yang⁸, Rouli Fang⁸, Kenji Watanabe⁹, Takashi Taniguchi¹⁰, B. J. Kim¹¹, Sang Hoon Chae⁸, Moon-Ho Jo^{1,2,11}, Angel Rubio⁴✉, Ofer Neufeld¹²✉ & Jonghwan Kim^{1,2,11}✉

Two-dimensional hexagonal materials such as transition metal dichalcogenides exhibit valley degrees of freedom, offering fascinating potential for valley-based quantum computing and optoelectronics. In nonlinear optics, the K and K' valleys provide excitation resonances that can be used for ultrafast control of excitons, Bloch oscillations, and Floquet physics. Under intense laser fields, however, the role of coherent carrier dynamics away from the K/K' valleys is largely unexplored. In this study, we observe quantum interferences in high harmonic generation from monolayer WS₂ as laser fields drive electrons from the valleys across the full Brillouin zone. In the perturbative regime, interband resonances at the valleys enhance high harmonic generation through multi-photon excitations. In the strong-field regime, the high harmonic generation is sensitively controlled by quantum interferences of laser-field-driven electrons occupying various points in the Brillouin zone, including regions far from the K/K' valleys. Our experimental observations are in strong agreement with quantum simulations, validating their interpretation. This work proposes new routes for harnessing laser-driven quantum interference in two-dimensional hexagonal systems and all-optical techniques to occupy and read-out electronic structures in the full Brillouin zone via strong-field nonlinear optics, advancing quantum technologies.

Under intense laser fields solids exhibit extreme nonlinear optical responses, such as high-harmonic generation (HHG)^{1,2}. Recently, HHG has been demonstrated in diverse material systems—superconductors³, Mott insulators^{4,5}, topological solids^{6–9}—and has garnered substantial interest as a powerful tool for exploring non-equilibrium quantum phenomena in condensed matter, including Bloch oscillations^{10,11}, charge coherence^{12,13}, and phonon dynamics^{14–16}. The initial step in HHG is the coherent excitation of electrons from the valence to the conduction bands, forming an electron-hole wave packet^{10,11,17–19}. Subsequently, two primary mechanisms contribute to

HHG: (1) interband transitions, which induce nonlinear optical polarizations via electron-hole recombination, and (2) intraband transitions, which generate laser-driven anharmonic currents. Two-dimensional (2D) hexagonal materials such as transition metal dichalcogenides provide a fascinating platform for investigating strong-field physics in solids. Due to the degenerate band gaps at the K and K' valleys—where nonzero Berry curvature arises—HHG is intimately connected to valley-specific excitations and all-optical readout^{20–24}. Interband excitation and recombination can be resonantly enhanced at the band edges by strong Coulomb interactions in atomically thin 2D structures^{20,25–27}.

A full list of affiliations appears at the end of the paper. ✉ e-mail: angel.rubio@mpsd.mpg.de; ofern@technion.ac.il; jonghwankim@postech.ac.kr

Intraband carrier dynamics also generate nonlinear anomalous and regular currents^{28,29}, enabling the reconstruction of the Berry curvature²⁸ and energy dispersions^{30–32} across the Brillouin zone (BZ). While bulk materials have shown that strong-field-driven quantum interference between interband and intraband excitation pathways can manipulate HHG^{11,33,34}, the corresponding effects in 2D hexagonal materials remain largely unexplored.

In the perturbative laser-field regime, local excitation near the K and K' valleys dominates the optical response, offering fundamental physical principles for valleytronic applications that utilize coherent valley-selective excitations as effective two-level systems³⁵. Although theoretical models often match experimental data under these conditions, they typically focus only on the valleys and ignore the more intricate band structure away from these high-symmetry points³⁵. On the other hand, when the laser field is sufficiently strong, excited carriers in the valleys can travel across the entire BZ, including to non-high-symmetry k-points with local energy minima or saddle points. While these alternative k-points do not benefit from valley-specific selection rules or minimal bandgap resonances, their coherent excitation under strong-field conditions can manipulate electrons for nonlinear optical applications similar to those in valleytronics, effectively forming a 2-level-like quantum system that can be controlled using light. Fully capturing these dynamics requires capabilities that drive excitation beyond the K/K' valleys and identify the unique spectral signatures associated with such extended electron–hole wave packets.

In this study, we investigate how HHG evolves in monolayer WS₂ as photo-excited carriers localized within valleys expand throughout the BZ. By irradiating WS₂ with mid-infrared pulses at 0.28 eV—resonant with a seven-photon transition to the optical gap—we initiate ultrafast carrier dynamics in the edges of the valence and conduction bands. Systematically increasing the laser intensity causes a transition to the non-perturbative regime, marked by nontrivial spectral features: (1) a pronounced kink in the harmonic yield's intensity dependence, and (2) a distinct spectral evolution that exhibits peak splitting and subsequent merging. Using ab-initio and model quantum mechanical simulations, we attribute these phenomena to quantum interference arising from laser-field-driven carrier motion transitioning from valley-localized states to highly delocalized states across the BZ, including the Γ and M points, as well as from interference between interband and intraband pathways. These findings provide a new mechanism to coherently populate and read out diverse electron–hole superpositions, expanding our ability to manipulate and probe the full BZ of 2D hexagonal solids. Our study thus provides insight that can pave new avenues in ultrafast valleytronics, ultrafast quantum information, and related fields.

Results and discussion

Transition from perturbative to strong-field driven HHG in monolayer WS₂

Figure 1a schematically illustrates the electronic processes in monolayer WS₂ initiated under intense laser driving. In the perturbative regime, nonlinear optical processes primarily arise from excitonic multiphoton transitions at the band gaps located at the K and K' valleys. Under intense laser fields, excitons become substantially delocalized through hybridization with higher excitonic bound states and continuum states³⁶. Eventually, ionized electrons and holes are driven far beyond the K and K' valleys over wide regions of momentum space, which opens additional pathways for higher-order nonlinear optical processes via intraband and interband transitions.

We fabricate large-area, high-quality, WS₂ monolayers using a gold-assisted exfoliation method³⁷. To further reduce external defects, the exfoliated monolayer WS₂ is encapsulated with hexagonal boron nitride on sapphire substrates via a dry transfer process³⁸. Our home-built femtosecond laser system provides linearly-polarized,

mid-infrared pulses with ~ 120 fs duration at 100 kHz repetition rate. We intentionally set the photon energy at ~ 0.28 eV (4500 nm) to match the 7-photon resonant exciton transition at the band edge. The laser power and polarization are precisely controlled and analyzed using polarization optics. HHG spectra are recorded with an electron-multiplying charge-coupled device to achieve a high signal-to-noise ratio. Owing to the combined advantages of high sample quality and high repetition rate, we can sensitively observe the quantum interference features from the perturbative to the non-perturbative regimes, as will be shown below. Additional details on sample preparation, laser setup, and a comparison of HHG spectra with and without hBN encapsulation are provided in the Supplementary Information (SI).

We now investigate HHG in monolayer WS₂ as a function the driving intensity. HHG signals are collected and integrated for both parallel and cross-polarization components with respect to the driving laser fields. HHG spectra exhibit markedly different profiles depending on the laser intensity (see Fig. 1b, c). At ~ 110 GW/cm² (red solid line in Fig. 1c), strong 7th harmonic signals are observed at 1.93 eV, while all other harmonic orders—including lower harmonic orders—are nearly absent. This selective enhancement arises from excitonic resonances at the K and K' valleys. The reflection contrast spectrum (Fig. 1e) and HHG spectrum (Fig. 1d) show absorption and photoluminescence peaks at 2 eV, respectively, originating from 1s exciton resonances at the optical gap. The 7th harmonic signal is located near 1s exciton resonances with a small detuning of 70 meV. Up to ~185 GW/cm² laser driving, the yield of 7th harmonic in Fig. 1f scale as $\propto I^7$ with respect to laser peak intensity (I). A similar intensity dependence is observed for photoluminescence under mid-infrared laser excitation (see SI), indicating that all optical processes observed in this regime are primarily mediated by the 7-photon transitions to the resonant excitonic state. Such excitonic enhancement has been experimentally reported for second harmonic generation in TMD monolayers and heterostructures^{39,40}. Recent theoretical studies predict that excitonic resonances can also strongly enhance high-order harmonic generation^{26,36,41,42}, in agreement with our experimental observations. At higher driving intensity (>185 GW/cm²), an HHG plateau spanning 5–11th harmonics emerges (Fig. 1b, c). Under these conditions, the HHG yield becomes non-perturbative, including for the 7th harmonic—the main observable analyzed in this study. Notably, Fig. 1f reveals a pronounced kink at ~200 GW/cm², which is not expected from the perturbative response, and which we will analyze with theory later on.

The crystal orientation dependence of the 7th harmonic yield also indicates the transition from the perturbative to the non-perturbative regime. Figure 2b–f present the integrated yield as a function of the angle between the laser field and the WS₂ zigzag direction (see the illustration in Fig. 2a). The crystal axis of WS₂ is determined from polarization analysis on even order harmonics (see SI). Polarization analysis confirms that the 7th harmonic is absent for the polarization component perpendicular to the driving laser field, as expected from HHG dynamical mirror-symmetry selection rules^{20,43} (see SI). At a laser intensity of ~ 125 GW/cm², dominated by the perturbative response from excitonic resonances, no apparent dependence on crystal orientation is observed (i.e., an isotropic response). However, in the non-perturbative regime, harmonic signals exhibit strong 60° periodic modulation, which becomes increasingly pronounced as the laser intensity rises from ~ 235 to 380 GW/cm², accompanied by significant changes in modulation depth and phase (with 60° periodicity, as expected from crystal symmetry⁴⁴)—Initially, polar plots show stronger harmonic yields along the armchair direction, but as the laser intensity increases the polar plot rotates by 30°, revealing stronger yields along the zigzag direction. Figure 2f is consistent with previous works^{20,21} in extreme laser intensities (>1 TW/cm²). The systematic modification of polar plots is indicative of a change in laser excitation

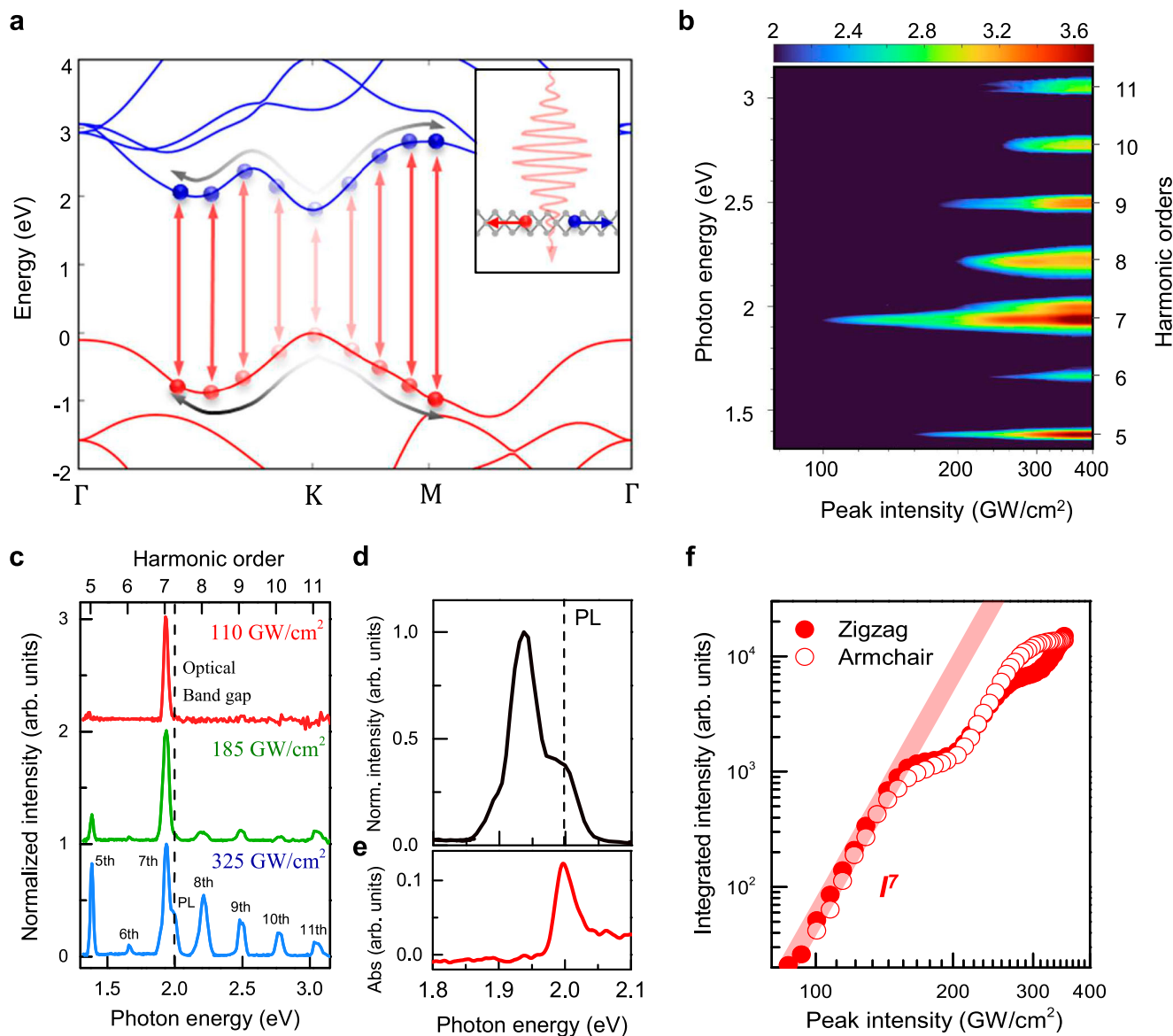


Fig. 1 | Non-perturbative response of lightwave-driven electron-hole pairs in monolayer WS₂. **a** Illustration of the electronic processes under strong laser excitation: Intense laser driving excites carriers throughout the BZ, and drives them in the respective bands. Interband recombination and intraband currents (red and gray arrows, respectively) emit HHG from various points in the BZ, including beyond K/K' valleys. In inset is an illustration of an electrons and holes driven by laser fields. **b** Experimentally measured HHG spectra as a function of laser intensity from 80 to 350 GW/cm². Note that harmonic yield in **(b)** is plotted in a logarithmic scale. The spectra display markedly different profiles in the perturbative and non-

perturbative regimes, showing onset of HHG plateau at higher driving, and the resonant 7th harmonic appearing in much lower intensities. **c** Line-cuts of HHG spectra from **(b)**. **d** Photoluminescence spectra showing clear excitonic signatures with 1s exciton resonance at 2 eV. **e** Reflection contrast spectrum indicating absorption near 2 eV, associated with the 1s exciton resonance. **f** Measured integrated 7th harmonic yield as a function of laser intensity (obtained from **(b)**), showing a kink feature arising for both zigzag and armchair orientations. Note that **(f)** is plotted in a logarithmic scale.

regime, and potentially also the physical mechanisms dominating HHG, as will be discussed below.

Laser intensity-dependent quantum interference in the 7th harmonic spectra

Figure 3c presents a 2D color map of high-spectral-resolution 7th harmonic spectra from monolayer WS₂ driven in the zig-zag direction as a function of laser intensity (nearly identical spectra are observed along the armchair direction, see SI). There are three key surprising results here, which form the main findings of this letter: (i) At ~150 GW/cm² where non-perturbative responses emerge from the laser-field-driven carriers, a very significant peak broadening arises. (ii) At slightly higher powers (~200 GW/cm²) multiple distinct peaks

emerge from the sharp peak that is characteristic of lower intensity driving. At yet higher intensities, ~250 GW/cm², these split peaks converge, resulting in a broader recombined spectral profile. (iii) This evolution is accompanied by a notable kink in the integrated yield of the 7th harmonic (see Fig. 1f and Fig. 3a) over the same laser intensity range, whereby the yield does not increase with increasing driving intensity.

In the perturbative regime, harmonic spectral profiles are primarily dictated by the driving pulse shape, typically exhibiting Gaussian-like profiles⁴³. Beyond the perturbative regime, however, the spectral profile can also be affected by interference between multiple quantum pathways of charge carriers that emerge on sub-laser-cycle timescales. Specifically, interference between distinct quantum

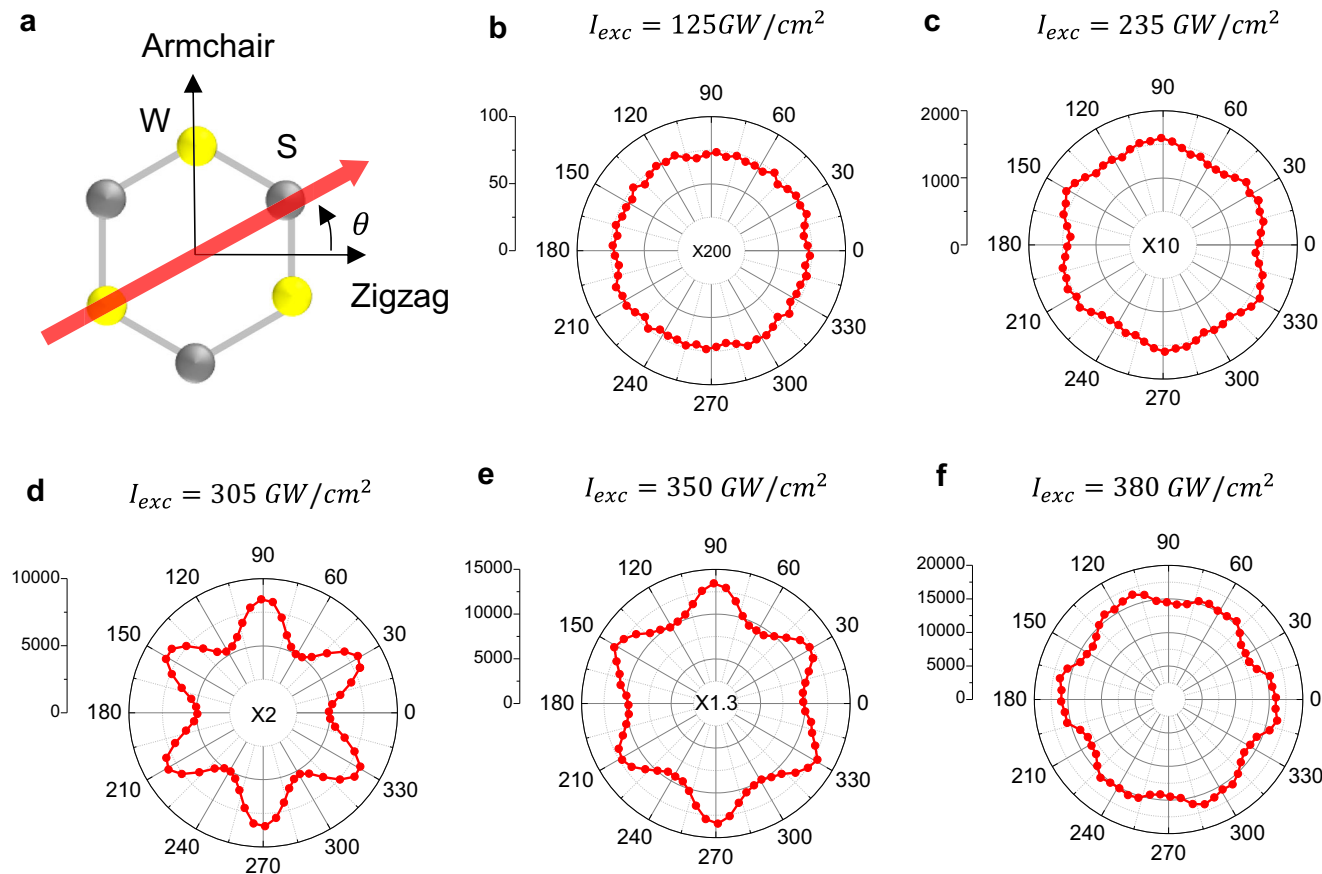


Fig. 2 | Crystal orientation dependence of the 7th harmonic generation yield. **a** Schematic of the monolayer WS₂ crystal structure and laser polarization axis (red arrow). The x(y)-axis corresponds to the zigzag (armchair) directions, respectively. The angle θ represents the counterclockwise rotation of the excitation laser polarization relative to the zigzag axis. **b–f** Crystal orientation dependence of seventh harmonics at increasing laser peak intensities: **b** 125 GW/cm², **c** 235 GW/cm², **d** 305 GW/cm², **e** 350 GW/cm², and **f** 380 GW/cm². For low driving power the

harmonic response is isotropic and perturbative. At higher intensity in the transition to non-perturbative HHG, a distinct six-fold pattern emerges with emission along the armchair direction. At yet higher intensity the six-fold pattern is slightly less pronounced and rotated by 30°, exhibiting stronger harmonic intensity along the zigzag direction. The harmonic signals in **(b)**, **(c)**, **(d)**, and **(e)** are magnified by factors of 200, 10, 2, and 1.3, respectively, to clearly visualize the pattern evolution at lower laser intensities.

pathways can produce spectral fringes, including peak splitting, that reflect the complex dynamics of charge carriers (as has been observed due to other mechanisms in bulk systems^{10,45–47}). Thus, we hypothesize that these phenomena all arise from multiple quantum path interferences. The main question is then which paths dominate the response of WS₂ in this regime?

To address this question, we perform exhaustive theoretical calculations based on several levels of theory. First, ab-initio time-dependent density functional theory (TDDFT) simulations are performed and compared with the experiment. Unfortunately, due to the very long-wavelength driving TDDFT fails to reproduce the dominant experimental features. This arises primarily because TDDFT does not include sufficient dephasing channels, which are highly relevant and can significantly alter the HHG spectra in our conditions⁴⁸ (because a single driving field period is ~ 15 fs, meaning dephasing occurs already within a single laser cycle, with recent dephasing times expected to be ~ fs on average⁴⁹). Nonetheless, the TDDFT simulations allow us to conclude that in our conditions contributions from electronic correlations and higher- or lower-order conduction and valence bands are expected to be minor in the overall response (see SI). Consequently, we develop a simple two-band model based on a tight-binding (TB) Hamiltonian (with an approach similar to that in refs. 50,51 see SI), which we employ in semiconductor Bloch equations (SBE) in the length gauge in a density

matrix formalism^{52,53} (given in a.u.):

$$\begin{aligned} \frac{\partial}{\partial t} \rho_{vv}(\mathbf{k}, t) &= i\mathbf{E}(t) \cdot [\mathbf{d}_{cv}(\mathbf{k}) \rho_{cv}^*(\mathbf{k}, t) - \mathbf{d}_{cv}^* \rho_{cv}(\mathbf{k}, t)] \\ \frac{\partial}{\partial t} \rho_{cv}(\mathbf{k}, t) &= -i \left[(\varepsilon_{CB}(\mathbf{k}(t)) - \varepsilon_{VB}(\mathbf{k}(t)) - \frac{i}{T_2}) \rho_{cv}(\mathbf{k}, t) \right. \\ &\quad \left. + \mathbf{E}(t) \cdot \left((\mathbf{d}_{cc}(\mathbf{k}) - \mathbf{d}_{vv}(\mathbf{k})) \rho_{cv}(\mathbf{k}, t) \right) \right. \\ &\quad \left. + \mathbf{d}_{cv}(\mathbf{k}) (2\rho_{vv}(\mathbf{k}, t) - 1) \right] \end{aligned} \quad (1)$$

where $\mathbf{k}(t) = \mathbf{k}_0 + \frac{1}{c} \mathbf{A}(t)$, with \mathbf{k}_0 the crystal momentum at $t = 0$, and $\mathbf{E}(t)$ the electric field vector (in the dipole approximation), which is connected to the vector potential via: $-\partial_t \mathbf{A}(t) = c\mathbf{E}(t)$, and c is the speed of light. In Eq. (1), ρ_{ij} is the density matrix, $\varepsilon_{CB}/\varepsilon_{VB}$ is the band eigen-energy, \mathbf{d}_{ij} are transition dipole matrix elements, and T_2 is the phenomenological dephasing time (taken as 5 fs⁴⁹). From the density matrix we obtain the time-dependent current, $\mathbf{J}(t) = \mathbf{J}_{\text{intra}}(t) + \mathbf{J}_{\text{inter}}(t)$ (separated to inter- intra-band contributions):

$$\begin{aligned} \mathbf{J}_{\text{intra}}(t) &= - \sum_{\mathbf{k} \in \text{BZ}} [\rho_{vv}(\mathbf{k}, t) \mathbf{p}_{vv}(\mathbf{k}(t)) + \rho_{cc}(\mathbf{k}, t) \mathbf{p}_{cc}(\mathbf{k}(t))] \\ \mathbf{J}_{\text{inter}}(t) &= - \sum_{\mathbf{k} \in \text{BZ}} 2\text{Re}[\rho_{cv}(\mathbf{k}, t) \mathbf{p}_{vc}(\mathbf{k}(t))] \end{aligned} \quad (2)$$

where \mathbf{p}_{ij} are the momentum matrix elements. All momentum and dipole matrix elements, as well as band energies, are obtained through

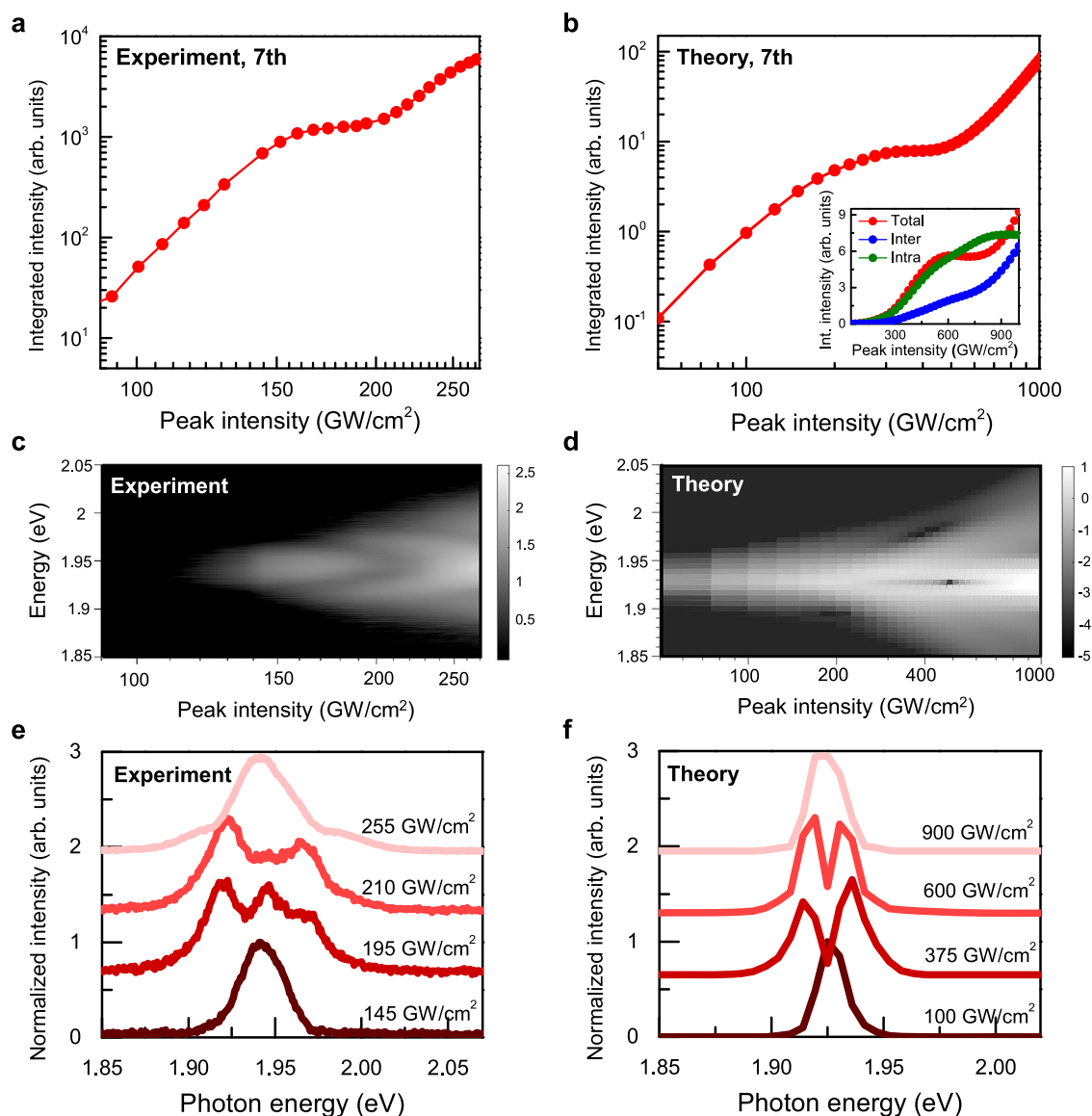


Fig. 3 | Quantum interference in harmonic generation. **a** The 7th harmonic yield vs. peak intensity in the zigzag direction (same as Fig. 1(f)). **b** Theoretical calculation of the 7th harmonic yield vs. peak intensity under laser excitation along the zigzag direction. We use a pulse duration of ~200 fs to resolve the peak splitting in (f). We confirm that nearly the same behavior is observed for a pulse duration of ~120 fs, corresponding to the actual experimental value (inset). The total current (red line) can be decomposed into intraband (green line) and interband (blue line) components, demonstrating that the kink arises from quantum interference between interband and intraband transitions. **c** Experimental and **d** theoretical 2D color map of the 7th harmonic spectra as a function of peak intensity under excitation along the zigzag direction, respectively. The color is plotted on a logarithmic scale. **e** Normalized 7th harmonic spectra at specific laser peak intensity corresponding to 145, 195, 210, and

255 GW/cm², which are linecuts of (c). At low laser field strength, a single peak is observed, but as the field strength increases, this single peak begins to broaden and split into multiple peaks, indicating the emergence of an interference between different electron pathways or transitions. As the field strength further increases to 255 GW/cm² and beyond, the formation of shoulder peaks becomes more pronounced potentially due to more complex quantum pathways or transitions. **f** Theoretical calculation of normalized 7th harmonic spectra at the specific laser peak intensity corresponding to 100, 375, 600 and 900 GW/cm², which is the linecut of (d). The calculated spectra exhibit interference patterns that closely resemble the experimental observations, particularly in the peak broadening and the emergence of multiple peaks at higher field strengths. All calculations were performed using the Tight Binding model, which was employed for solving the Semiconductor Bloch Equations.

analytical expressions from the TB Hamiltonian, which is optimally fitted to DFT bands throughout across entire BZ with an accurate 14th-order nearest-neighbor Hamiltonian (where spin is neglected and with the gap at K/K' offset to match experimental values, as it is often underestimated in DFT). From $J(t)$ we compute the HHG spectrum as $I_{\text{HHG}}(\Omega) = |\int dt f(t) \partial_t J(t) e^{-i\Omega t}|^2$, with $f(t)$ being a super-gaussian window function. For all additional technical details of the propagation and numerical procedures see the SI.

Figure 3b, d, f present numerical results employing the SBE-TB formalism, showing strong agreement with the experiment. The simulations correctly predict the kink in the 7th harmonic yield vs. peak

intensity (Fig. 3d). A pulse duration of ~200 fs is employed to resolve the peak splitting in Fig. 3d. In the inset of Fig. 3d, we confirm that nearly the same behavior is observed for a pulse duration of ~120 fs, corresponding to the actual experimental value. The total current (red line) can be decomposed into intraband (green line) and interband (blue line) components, elucidating that this effect originates from quantum interference between interband and intraband emission channels—a feature absent in either channel alone and requiring their complete or partial destructive interference. This is the first observation to our knowledge of such clear interferences in 2D systems. We note that the onset intensity of this effect is overall higher in the theory, likely due to

excitonic effects not captured in our simulations. Excitonic resonances can enhance carrier excitation even at lower laser intensities. Strong Coulomb interactions also give rise to tightly bound excitons in real space, which in turn promote greater momentum-space delocalization of excited photo-carriers, even without laser-field-driven intraband excitations. According to recent studies⁵⁴, exciton–phonon and exciton–plasmon scattering processes can provide finite momentum to the carriers. Furthermore, strong-laser-field-driven exciton ionization processes³⁶ can open additional HHG pathways that are not captured by the current theory. To accurately address the issues above, time-resolved photoemission spectroscopy or time-resolved absorption spectroscopy under identical mid-infrared excitation can provide direct access to the probe excitonic states and carrier scattering dynamics in the time domain. However, such an investigation goes beyond the scope of the present study.

Theoretical analysis of HHG in monolayer WS₂

At the next stage, our theory reproduces the peak broadening and splitting dynamics vs. laser intensity (see Fig. 3a–d)). Note that here we employed much longer driving laser pulses in order to obtain sufficient spectral resolution (~200 fs FWHM), but otherwise employed the same conditions as in the experiment. In the simulations, such long time-scale dynamics are necessary to be able to resolve peak splitting on an energy scale of ~0.02 eV. Our theoretical analysis reveals that the splitting and converging dynamics do not arise solely due to interference of interband and intraband channels, as the effect appears in each channel separately (see SI for 7th harmonic spectrum from interband and intraband channels). To gain further insight, we perform a comprehensive *k*-resolved analysis of the HHG yield, and uncover that at the onset of the peak splitting, a substantial portion of the BZ is excited (comparing occupations in Fig. 4a, b, middle panel). Indeed, at high laser powers, electrons occupy not only regions near *K/K'* valleys, but also towards Γ and *M* points. The HHG emission from these regions is comparable to that from the *K/K'* valleys and, under certain conditions, can be even stronger. Mathematically, this is clear due to the relatively low optical gap throughout the BZ (e.g., the gap at Γ is ~3 eV, only ~1 eV higher than the gap at *K/K'*). The detailed spectral profiles are determined by the magnitudes and phases of the HHG emission, which depend on specific laser excitation conditions including finite beam size, temporal and spectral pulse profiles^{45,55}. Nevertheless, this result clearly indicates that the peak splitting originates from quantum interference of laser-field-driven carriers occupying multiple *k*-points including regions near Γ and *M* points.

This conclusion is further validated by performing additional simulations where the TB Hamiltonian is modified to reproduce the correct electronic structure only near *K/K'* valleys, while the gap is artificially increased towards Γ and *M* to suppress their contribution (see right panels in Fig. 4b, c). Indeed, in these conditions, the peak splitting phenomena are completely suppressed at identical laser power, corroborating that interference of emission between different points in the BZ accounts for the physical mechanism of peak splitting (and that specifically the *K/K'* valleys, including their Berry curvature, cannot alone account for the effect). The peak closing dynamics at yet higher driving is seen to arise due to increased dominance of the intraband emission channel where the split peak converges.

Discussion

In conclusion, we studied HHG in WS₂ monolayers with tunable long-wavelength laser driving. We identified a transition from perturbative HHG—dominated by bound excitons and valley-confined carriers with near-isotropic orientation dependence—to a strong-field regime characterized by delocalized carrier dynamics across the BZ and pronounced anisotropic orientation dependence. In the perturbative regime, exciton resonances strongly enhance the 7th harmonic near the 1 s exciton resonance. As the laser intensity grows, ionized carriers

take over, producing nontrivial spectral features such as splitting and multiple kinks in the HHG yield. These experimentally observed, and theoretically validated, phenomena, signify the activation of new quantum pathways in intense fields. Our quantum simulations, including *k*-resolved analysis, reveal that these effects result from quantum interference between interband and intraband transitions, as well as quantum interference of laser-field-driven carriers occupying multiple points in the BZ along the laser driving axis. These findings expand our understanding of ultrafast carrier dynamics in valley-based 2D materials and demonstrate the power of HHG for probing light–matter interactions in 2D hexagonal systems.

Especially, we note that these are the first signatures of such interference phenomena in 2D systems, offering a direct all-optical pathway to not only to selectively excite electrons in various high/low-symmetry points of the hexagonal BZ (beyond *K/K'*, also Γ and *M*), but also read them out as clear spectral interference signatures in HHG. Thus, this work paves the way for the next generation of optoelectronic and quantum devices capable of operating at petahertz frequencies, and utilizing multiple *k*-points beyond valleytronics for mimicking 2-level quantum systems.

Methods

Sample fabrication

A high-quality monolayer WS₂ sample was prepared by the gold-assisted exfoliation method. A 150 nm thickness gold layer was deposited on a flat silicon substrate with a 90 nm thick oxide layer. A polyvinylpyrrolidone (PVP) solution (Sigma Aldrich, mw 40000, 10% wt in ethanol/acetonitrile wt 1/1) was spin-coated on the top of the Au film and cured at 150 °C for 5 min. This PVP layer served as a sacrificial layer to prevent contamination from tape residue. The prepared PVP/Au was picked up with thermal release tape (TRT), revealing an ultra-flat, clean, and fresh gold surface—referred to as the gold tape. The gold tape is pressed onto a freshly cleaved bulk WS₂ crystal (HQ graphene). As the tape is lifted off the surface, it carries the PVP/Au layer with a monolayer WS₂ crystal attached to the Au surface. And then it is further transferred onto a silicon substrate with a 90 nm thick oxide layer. The TRT is removed by heating at 135 °C. The PVP layer is removed by dissolving in deionized (DI) water for 2 h. Finally, the sample on the substrate, covered by Au layer, was rinsed with acetone and cleaned by O₂ plasma for 4 min to remove any remaining PVP polymer residues. We note that WS₂ monolayers are not directly exposed to the O₂ plasma during this step because the WS₂ monolayers are protected by the Au film. Finally, the Au layer is dissolved in a KI/I₂ gold etchant solution and then the monolayer TMD is rinsed with DI water and isopropanol.

The van der Waals heterostructure of WS₂ monolayer and hBN was prepared by the dry transfer technique³⁸. The thickness of WS₂ monolayer was first identified by the optical contrast of a microscope image, followed by the detailed spectroscopic characterization. Approximately 20 nm-thick hBN flakes were exfoliated onto a silicon substrate with 90 nm oxide layer. To fabricate the encapsulated WS₂ monolayer, we used the thermoplastic methacrylate copolymer (Elvacite 2552 C, Lucite International) stamp to pick up the hBN flakes and WS₂ monolayer in sequence with accurate alignment based on an optical microscope. The Elvacite stamp with the heterostructure was then stamped onto a sapphire substrate. The polymer and samples were heated up at 70 °C for the pick-up and 200 °C for the stamp process, respectively. Finally, we dissolved the Elvacite in acetone for 3 min at 100 °C.

HHG measurements

Mid-infrared pulses were generated from a femtosecond laser system (Light Conversion PHAROS) using an optical parametric amplifier (ORPHEUS) and a difference frequency generator (LYRA). The output served wavelength-tunable multi-cycle pulses with a repetition rate of 100 kHz. The fundamental laser wavelength is set at 4.5 μ m, that can

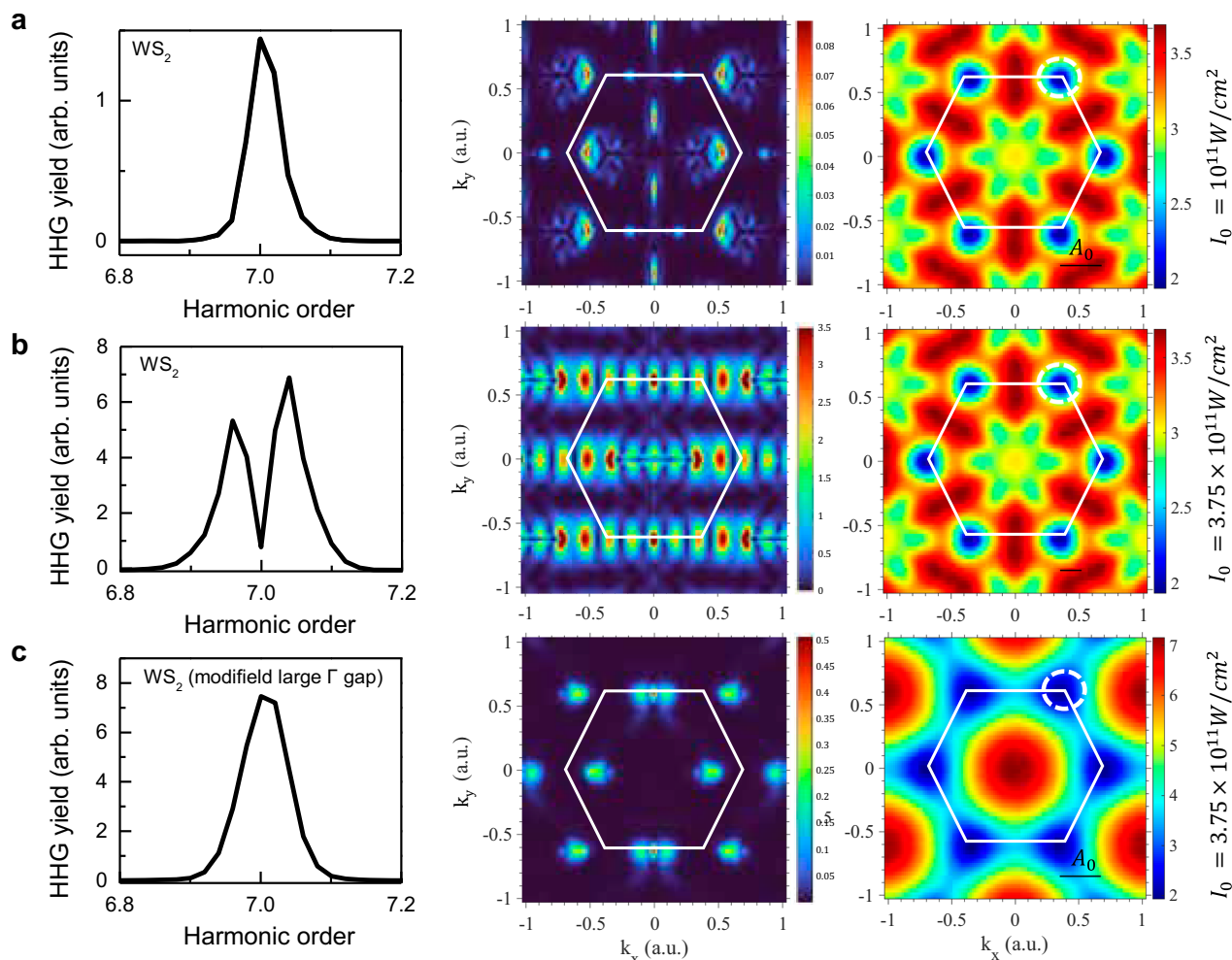


Fig. 4 | Theory of peak splitting in HHG from WS₂. **a** SBE simulated 7th harmonic spectrum (left), showing no onset of peak splitting at lower power (100 GW/cm²). Middle panel shows the k-resolved contributions to this peak, indicating mostly localized charge carrier excitation and emission from the K/K' valleys. Right panel shows the optical gap throughout the BZ in this system. The color is plotted on a linear scale for both middle and right panel. **b** Same as (a) for higher driving power (375 GW/cm²) where there is peak-splitting occurring. Here, emission is contributed

form delocalized regions in the BZ, including from Γ and M. The evenly spaced interference pattern in k-space presumably indicates regions with constructive/destructive interference due to the phase of the harmonic emission. **c** Same as (b) but with the modified TB model (see text) that reproduced the electronic structure in WS₂ only near the K/K' valleys (see right panel), where peak splitting does not occur. The white hexagon shows the outline of the first Brillouin zone edge.

avoid strong CO₂ absorption bands. The spectral linewidth of the pulse is estimated to be 15.4 meV in full width at half maximum (FWHM), and the pulse duration was estimated to be 120 fs, assuming a Fourier-transform-limited pulse. Laser intensity was precisely controlled by a pair of linear polarizers inserted into the beam path. Half-wave plates were also inserted into the beam path to control the polarization of the excitation laser. The mid-infrared pulses were then focused near the center of the monolayer WS₂ sample using ZnSe focusing objectives, producing a spot size of approximately 30–80 μ m. The emitted HHG was collected by a 50 \times objective lens in a transmission geometry, and its polarization was analyzed by a half-wave plate mounted on a motorized stage and a fixed Glan-Taylor polarizer. The HHG spectra were recorded by an electron-multiplying charge-coupled device detector (ProEM, Princeton Instruments) and a grating spectrometer (SP-2300, Princeton Instruments) at Materials Imaging & Analysis Center of POSTECH.

Data availability

All of the data that support the findings of this study are available in the main text or Supplementary Information. Source data are available from the corresponding authors on request.

Code availability

TDDFT simulations were performed on Octopus code, which is freely available and is open access. Additional information can be obtained from the corresponding authors upon request.

References

- Ghimire, S. et al. Observation of high-order harmonic generation in a bulk crystal. *Nat. Phys.* **7**, 138–141 (2011).
- Ghimire, S. & Reis, D. A. High-harmonic generation from solids. *Nat. Phys.* **15**, 10–16 (2019).
- Alcalà, J. et al. High-harmonic spectroscopy of quantum phase transitions in a high-T_c superconductor. *Proc. Natl Acad. Sci. USA* **119**, e2207766119 (2022).
- Orthodoxou, C., Zair, A. & Booth, G. H. High harmonic generation in two-dimensional Mott insulators. *npj Quantum Mater.* **6**, 76 (2021).
- Murakami, Y., Eckstein, M. & Werner, P. High-harmonic generation in mott insulators. *Phys. Rev. Lett.* **121**, 057405 (2018).
- Bai, Y. et al. High-harmonic generation from topological surface states. *Nat. Phys.* **17**, 311–315 (2021).
- Heide, C. et al. Probing topological phase transitions using high-harmonic generation. *Nat. Photon.* **16**, 620–624 (2022).

8. Schmid, C. P. et al. Tunable non-integer high-harmonic generation in a topological insulator. *Nature* **593**, 385–390 (2021).
9. Neufeld, O., Tancogne-Dejean, N., Hübener, H., De Giovannini, U. & Rubio, A. Are there universal signatures of topological phases in high-harmonic generation? Probably not. *Phys. Rev. X* **13**, 031011 (2023).
10. Reislöhner, J., Kim, D., Babushkin, I. & Pfeiffer, A. N. Onset of Bloch oscillations in the almost-strong-field regime. *Nat. Commun.* **13**, 7716 (2022).
11. Schubert, O. et al. Sub-cycle control of terahertz high-harmonic generation by dynamical Bloch oscillations. *Nat. Photon* **8**, 119–123 (2014).
12. Heide, C. et al. Probing electron-hole coherence in strongly driven 2D materials using high-harmonic generation. *Optica* **9**, 512–516 (2022).
13. Freudenstein, J. et al. Attosecond clocking of correlations between Bloch electrons. *Nature* **610**, 290–295 (2022).
14. Neufeld, O., Zhang, J., De Giovannini, U., Hübener, H. & Rubio, A. Probing phonon dynamics with multidimensional high harmonic carrier-envelope-phase spectroscopy. *Proc. Natl Acad. Sci.* **119**, e2204219119 (2022).
15. Zhang, J. et al. High-harmonic spectroscopy probes lattice dynamics. *Nat. Photon.* **18**, 792–798 (2024).
16. Rana, N., Mrudul, M. S., Kartashov, D., Ivanov, M. & Dixit, G. High-harmonic spectroscopy of coherent lattice dynamics in graphene. *Phys. Rev. B* **106**, 064303 (2022).
17. Wu, M., Ghimire, S., Reis, D. A., Schafer, K. J. & Gaarde, M. B. High-harmonic generation from Bloch electrons in solids. *Phys. Rev. A* **91**, 043839 (2015).
18. Vampa, G. et al. Theoretical analysis of high-harmonic generation in solids. *Phys. Rev. Lett.* **113**, 073901 (2014).
19. Yue, L. & Gaarde, M. B. Introduction to theory of high-harmonic generation in solids: tutorial. *J. Opt. Soc. Am. B* **39**, 535–555 (2022).
20. Yoshikawa, N. et al. Interband resonant high-harmonic generation by valley polarized electron-hole pairs. *Nat. Commun.* **10**, 3709 (2019).
21. Liu, H. et al. High-harmonic generation from an atomically thin semiconductor. *Nat. Phys.* **13**, 262–265 (2017).
22. Jiménez-Galán, Á., Silva, R. E. F., Smirnova, O. & Ivanov, M. Sub-cycle valleytronics: control of valley polarization using few-cycle linearly polarized pulses. *Optica* **8**, 277–280 (2021).
23. Mrudul, M. S., Jiménez-Galán, Á., Ivanov, M. & Dixit, G. Light-induced valleytronics in pristine graphene. *Optica* **8**, 422 (2021).
24. Neufeld, O., Hübener, H., Jotzu, G., De Giovannini, U. & Rubio, A. Band nonlinearity-enabled manipulation of Dirac nodes, Weyl cones, and valleytronics with intense linearly polarized light. *Nano Lett.* **23**, 7568–7575 (2023).
25. Hader, J., Neuhaus, J., Moloney, J. V. & Koch, S. W. Coulomb enhancement of high harmonic generation in monolayer transition metal dichalcogenides. *Opt. Lett.* **48**, 2094 (2023).
26. Molinero, E. B. et al. Subcycle dynamics of excitons under strong laser fields. *Sci. Adv.* **10**, eadn6985 (2024).
27. Chang Lee, V., Yue, L., Gaarde, M. B., Chan, Y. & Qiu, D. Y. Many-body enhancement of high-harmonic generation in monolayer MoS₂. *Nat. Commun.* **15**, 6228 (2024).
28. Luu, T. T. & Wörner, H. J. Measurement of the Berry curvature of solids using high-harmonic spectroscopy. *Nat. Commun.* **9**, 916 (2018).
29. Yue, L. & Gaarde, M. B. Characterizing anomalous high-harmonic generation in solids. *Phys. Rev. Lett.* **130**, 166903 (2023).
30. Vampa, G. et al. All-optical reconstruction of crystal band structure. *Phys. Rev. Lett.* **115**, 193603 (2015).
31. Borsch, M. et al. Super-resolution lightwave tomography of electronic bands in quantum materials. *Science* **370**, 1204–1207 (2020).
32. Lanin, A. A., Stepanov, E. A., Fedotov, A. B. & Zheltikov, A. M. Mapping the electron band structure by intraband high-harmonic generation in solids. *Optica* **4**, 516 (2017).
33. Hohenleutner, M. et al. Real-time observation of interfering crystal electrons in high-harmonic generation. *Nature* **523**, 572–575 (2015).
34. Tancogne-Dejean, N., Mücke, O. D., Kärtner, F. X. & Rubio, A. Ellipticity dependence of high-harmonic generation in solids originating from coupled intraband and interband dynamics. *Nat. Commun.* **8**, 745 (2017).
35. Schaibley, J. R. et al. Valleytronics in 2D materials. *Nature Reviews. Materials* **1**, 16055 (2016).
36. Kobayashi, Y. et al. Floquet engineering of strongly driven excitons in monolayer tungsten disulfide. *Nat. Phys.* <https://doi.org/10.1038/s41567-022-01849-9> (2023).
37. Liu, F. et al. Disassembling 2D van der Waals crystals into macroscopic monolayers and reassembling into artificial lattices. *Science* **367**, 903–906 (2020).
38. Wang, L. et al. One-dimensional electrical contact to a two-dimensional material. *Science* **342**, 614–617 (2013).
39. Wang, G. et al. Giant enhancement of the optical second-harmonic emission of WSe_2 monolayers by laser excitation at exciton resonances. *Phys. Rev. Lett.* **114**, 097403 (2015).
40. Shree, S. et al. Interlayer exciton mediated second harmonic generation in bilayer MoS₂. *Nature. Communications* **12**, 6894 (2021).
41. Jensen, S. V. B., Madsen, L. B., Rubio, A. & Tancogne-Dejean, N. High-harmonic spectroscopy of strongly bound excitons in solids. *Phys. Rev. A* **109**, 063104 (2024).
42. Chang Lee, V., Yue, L., Gaarde, M. B., Chan, Y. & Qiu, D. Y. Many-body enhancement of high-harmonic generation in monolayer MoS₂. *Nature. Communications* **15**, 6228 (2024).
43. Shen, Y. R. *The Principles of Nonlinear Optics*. (Wiley, 2003).
44. Neufeld, O., Podolsky, D. & Cohen, O. Floquet group theory and its application to selection rules in harmonic generation. *Nat. Commun.* **10**, 405 (2019).
45. Xia, P. et al. High-harmonic generation in GaAs beyond the perturbative regime. *Phys. Rev. B* **104**, L21202 (2021).
46. Sekiguchi, F. et al. Enhancing high harmonic generation in GaAs by elliptically polarized light excitation. *Phys. Rev. B* **108**, 205201 (2023).
47. Kim, Y. W. et al. Spectral interference in high harmonic generation from solids. *ACS Photonics* **6**, 851–857 (2019).
48. Kim, Y. et al. Dephasing dynamics accessed by high harmonic generation: determination of electron-hole decoherence of Dirac fermions. *Nano Lett.* **24**, 1277–1283 (2024).
49. Korolev, V. et al. Unveiling the Role of Electron-Phonon Scattering in Dephasing High-Order Harmonics in Solids. *arXiv preprint arXiv:2401.12929* (2024).
50. Wang, Y. et al. Tight-binding model for electronic structure of hexagonal boron phosphide monolayer and bilayer. *J. Phys.: Condens. Matter* **31**, 285501 (2019).
51. Galler, A., Rubio, A. & Neufeld, O. Mapping light-dressed Floquet bands by highly nonlinear optical excitations and valley polarization. *J. Phys. Chem. Lett.* **14**, 11298–11304 (2023).
52. Yue, L. & Gaarde, M. B. Structure gauges and laser gauges for the semiconductor Bloch equations in high-order harmonic generation in solids. *Phys. Rev. A* **101**, 053411 (2020).
53. Mrudul, M. S. & Dixit, G. High-harmonic generation from monolayer and bilayer graphene. *Phys. Rev. B* **103**, 094308 (2021).
54. Madéo, J. et al. Directly visualizing the momentum-forbidden dark excitons and their dynamics in atomically thin semiconductors. *Science* **370**, 1199–1204 (2020).
55. Floss, I. et al. Ab initio multiscale simulation of high-order harmonic generation in solids. *Phys. Rev. A* **97**, 011401 (2018).

Acknowledgements

We acknowledge fruitful discussions with Prof. Dieter Bauer, Prof. Marcelo Ciappinna, Prof. Gopal Dixit, and Dr. Lun Yue. This work was supported by the Institute for Basic Science (IBS), Korea under Project Code IBS-R014-A1. J.K. acknowledge the support from the National Research Foundation of Korea grants (NRF-2023R1A2C2007998). This study was also supported by the MSIT (Ministry of Science and ICT), Korea, under the ITRC (Information Technology Research Center) support program (IITP-2023-RS-2022-00164799) supervised by the IITP (Institute for Information & Communications Technology Planning & Evaluation). This work was supported by the European Research Council (ERC-2015-AdG694097), the Cluster of Excellence 'Advanced Imaging of Matter' (AIM), Grupos Consolidados (IT1453-22), and Deutsche Forschungsgemeinschaft (DFG)-SFB-925-project 170620586. The Flatiron Institute is a division of the Simons Foundation. We acknowledge support from the Max Planck-New York City Center for Non-Equilibrium Quantum Phenomena. A.C. acknowledges partial support by the Sistema Nacional de Investigación de Panamá. A.G. acknowledges support by the Austrian Science Fund (FWF) grant 10.55776/V988. S.H.C. acknowledges funding from the A*STAR, Singapore, Advanced Manufacturing and Engineering (AME) Individual Research Grant (IRG) under the Project M23M6c0109. This work is supported by the MOE AcRF Tier 3 grant (MOE-MOET32023-0003) "Quantum Geometric Advantage" and the Nanyang NanoFabrication Center (N2FC). K.W. and T.T. acknowledge support from the JSPS KAKENHI (Grant Numbers 21H05233 and 23H02052), the CREST (JPMJCR24A5), JST and World Premier International Research Center Initiative (WPI), MEXT, Japan.

Author contributions

J.K., O.N., and A.R. conceived the project. M.K. built the optical setup and, together with T.K., obtained the HHG spectra. T.K., X.G., Y.Y., and R.F. fabricated the monolayer WS₂ samples using Au-assisted exfoliation. K.W. and T.T. provided the hBN crystals used for encapsulation. O.N., A.G., and D.K. carried out theoretical calculations. M.K., T.K., A.G., D.K., A.C., B.J.K., S.H.C., M.-H.J., A.R., O.N., and J.K. analyzed the HHG data. All authors discussed the results and contributed to writing the manuscript.

Competing interests

The authors declare no competing interests.

Additional information

Supplementary information The online version contains supplementary material available at <https://doi.org/10.1038/s41467-025-65725-9>.

Correspondence and requests for materials should be addressed to Angel Rubio, Ofer Neufeld or Jonghwan Kim.

Peer review information *Nature Communications* thanks the anonymous reviewers for their contribution to the peer review of this work. A peer review file is available.

Reprints and permissions information is available at <http://www.nature.com/reprints>

Publisher's note Springer Nature remains neutral with regard to jurisdictional claims in published maps and institutional affiliations.

Open Access This article is licensed under a Creative Commons Attribution-NonCommercial-NoDerivatives 4.0 International License, which permits any non-commercial use, sharing, distribution and reproduction in any medium or format, as long as you give appropriate credit to the original author(s) and the source, provide a link to the Creative Commons licence, and indicate if you modified the licensed material. You do not have permission under this licence to share adapted material derived from this article or parts of it. The images or other third party material in this article are included in the article's Creative Commons licence, unless indicated otherwise in a credit line to the material. If material is not included in the article's Creative Commons licence and your intended use is not permitted by statutory regulation or exceeds the permitted use, you will need to obtain permission directly from the copyright holder. To view a copy of this licence, visit <http://creativecommons.org/licenses/by-nc-nd/4.0/>.

© The Author(s) 2025

¹Department of Materials Science and Engineering, Pohang University of Science and Technology, Pohang, Republic of Korea. ²Center for van der Waals Quantum Solids, Institute for Basic Science (IBS), Pohang, Republic of Korea. ³Institute of Theoretical and Computational Physics, Graz University of Technology, Graz, Austria. ⁴Max Planck Institute for the Structure and Dynamics of Matter, Hamburg, Germany. ⁵Departamento de Física, Área de Física, Universidad de Panamá, Ciudad Universitaria 3366 Octavio Mendez Pereira, Panama City, Panama. ⁶Sistema Nacional de Investigación, Clayton Panama, Panama. ⁷Parque Científico y Tecnológico, Universidad Autónoma de Chiriquí, Ciudad Universitaria, David, Panama. ⁸School of Electrical and Electronics Engineering, School of Materials Science and Engineering, Nanyang Technological University, Singapore, Singapore. ⁹Research Center for Electronic and Optical Materials, National Institute for Materials Science, Tsukuba, Japan. ¹⁰Research Center for Materials Nanoarchitectonics, National Institute for Materials Science, Tsukuba, Japan. ¹¹Department of Physics, Pohang University of Science and Technology, Pohang, Republic of Korea. ¹²Technion Israel Institute of Technology, Faculty of Chemistry, Haifa, Israel. ¹³These authors contributed equally: Minjeong Kim, Taeho Kim, Anna Galler. ✉ e-mail: angel.rubio@mpsd.mpg.de; ofern@technion.ac.il; jonghwankim@postech.ac.kr